Applied Catalysis B: Environmental 268 (2020) 118385

Contents lists available at ScienceDirect

Applied Catalysis B: Environmental

journal homepage: www.elsevier.com/locate/apcatb

Pressure-driven catalyst synthesis of Co-doped Fe_3C@Carbon nano-onions for efficient oxygen evolution reaction

Shishuai Xu[a,b,1], Mingzhi Wang[a,1], Govindarajan Saranya[c,1], Ning Chen[d], Lili Zhang[e], Yan He[e], Lailei Wu[a], Yutong Gong[f,**], Zhiqiang Yao[g], Gongkai Wang[h], Zhibin Wang[i], Shijing Zhao[b], Hu Tang[b], Mingyang Chen[j,**], Huiyang Gou[b,i,*]

[a] State Key Laboratory of Metastable Materials Science and Technology, Yanshan University, Qinhuangdao 066004, China
[b] Center for High Pressure Science and Technology Advanced Research, Beijing 100094, China
[c] Beijing Computational Science Research Center, Beijing 100193, China
[d] Canadian Light Source Saskatoon, Saskatchewan S7N2V3, Canada
[e] Shanghai Synchrotron Radiation Facility, Shanghai Advanced Research Institute, Chinese Academy of Sciences, China
[f] International Center for Materials Discovery, School of Materials Science and Engineering, Northwestern Polytechnical University, Xi'an, 710072, China
[g] School of Materials Science and Engineering and International Joint Research Laboratory for Low-Carbon & Environmental Materials of Henan Province, Zhengzhou University, Zhengzhou 10459, China
[h] School of Material Science & Engineering, Research Institute for Energy Equipment Materials, Hebei University of Technology, Tianjin, 300130, China
[i] College of Environment and Chemical Engineering, Yanshan University, Qinhuangdao 066004, China
[j] Center for Green Innovation, School of Materials Science and Engineering, University of Science and Technology Beijing, Beijing 100083, China

ARTICLE INFO

Keywords:
Electrocatalysis
Oxygen evolution reaction
Co-doped Fe_3C@ carbon nano-onions
High pressure synthesis

ABSTRACT

Optimization of electrocatalytic performance and identification of active sites for water splitting catalysts are important for the renewable energy technologies. Using one-step facile high-pressure annealing approach, herein, we report the rapid synthesis and preferred selections of 3*d* transition metals M (Mn, Co, and Ni)-doped Fe_3C@carbon nano-onions[2] for optimized electrocatalytic performance. The as-prepared highly crystalline and spheroidal core-shell-like FCC@CNOs exhibits an excellent OER activity with overpotential of 271 mV at 10 mA cm^{-2} among carbides catalysts, and long-term stability over 40 h (100 mA cm^{-2}). Both experimental and density functional theory results support that the synergistic interaction of Fe and Co atom promotes FCC@CNOs having lower OER kinetic barrier and surface Co sites are activated for improved performance, not a conventional additive effect of bimetallic Co and Fe atoms. The present study provides the insights on the direct understanding of the synergistic effect of bimetallic electrocatalyts and identification of real active sites.

1. Introduction

Developing high-performance catalyst and recognizing active sites are ultimate goals for catalysis. Generally, discovery of high-performance catalysts relies heavily on the "trial and error" development cycles, for which high-efficient and time-saving synthetic strategies are highly desired. On the other hand, determination of active sites for deep understanding of catalysis remains great challenges, most of the high-efficient catalysts, especially the electrochemical catalysts, are complicated in structure, which highlight the strong need for developing structurally-simple catalysts. Therefore, developing effective strategy to obtain superior catalysts with uniform or simple structure is of great significance to achieve the ultimate targets, which may influence the sustainable energy solutions.

Electrochemical water splitting is a very promising technology to alleviate global energy and environmental crisis [1,2]. Oxygen evolution reaction (OER), the anode reaction in water splitting devices, involves the multi-step electron transfer paths and requires substantial overpotentials [3,4]. Therefore, it is of tremendous interest to develop low-cost, stable and highly active alternatives for practical applications to minimize the usage of scarce and less stable noble metal-based catalyst, *e.g.,* RuO_2, IrO_2 [5]. Transition metal carbides (TMCs) have

* Corresponding author at: Center for High Pressure Science and Technology Advanced Research, Beijing 100094, China.
** Corresponding authors.
E-mail addresses: gongyutong@nwpu.edu.cn (Y. Gong), mychen@ustb.edu.cn (M. Chen), huiyang.gou@hpstar.ac.cn (H. Gou).
[1] These authors have contributed equally to this work.
[2] M-doped Fe_3C@carbon nano-onions (Mn, Co, and Ni) are abbreviated as FMC@CNOs, FCC@CNOs and FNC@CNOs.

https://doi.org/10.1016/j.apcatb.2019.118385
Received 7 August 2019; Received in revised form 12 October 2019; Accepted 2 November 2019
Available online 04 November 2019
0926-3373/

shown their good prospect by their high mechanical stability, excellent corrosion resistance, high conductivities and well-behaved catalytic properties [6–8]. In particular, Fe_3C@NCNTs-NCNFs is found to exhibit a high OER performance due to unique 3D hierarchical architecture [9]. FeS/Fe_3C@ N-S -C is displayed an efficient trifunctional electrocatalytic activity owing to the synergistic interaction between FeS and Fe_3C in N-S co-doping carbons with nanostructures [10]. Fe_3C@Fe,N,S-GCM nanocomposite shows a high OER electrocatalytic activity, due to the synergy effect of Fe_3C, Fe-N_x and N,S-co-doped carbon active sites [11]. It has also been shown that secondary 3*d*-transition metals could help increase the catalytic performance of cementites [12–17]. Despite these successes, the complex composition of developed composites restricts the identification of the actual active sites for carbide catalysts.

Traditionally, TMCs-based and carbon-derivative OER catalysts are often synthesized via gas-solid reaction, solid-liquid or solid-state reaction [18]. For example, Fe/Fe_3C embedded CNT/CNS was synthesized by thermally activating MOF (ZIF-Zn^{2+} and MIL-Fe^{3+}) [19]. A pea-like architecture CoP-Mo_2C@NC/CC was prepared via the solvothermal method followed phosphidation [20]. Co-FeCo/N-G was obtained by microwave plasma enhanced chemical vapor deposition [21]. $Co_{1-x}Ni_xS_2$-NGO was synthesized by hydrothermal process in Teflon-lined stainless-steel autoclave [22]. However, those routes often suffer from long synthetic cycles, complex procedures and uncontrolled composition, which lead to great difficulties in catalyst screening or mechanism understanding. As a consequence, an efficient synthetic protocol which can provide catalysts with high crystallinity and uniform structure, especially surface structure where catalysis occurs, is of vital importance to identify the real active sites and study the doping effects in carbide-based OER catalysts. High pressure (HP) annealing method has been recognized to be an effective approach for rapidly realizing the pure, homogeneous and high crystallinity materials with excellent chemical and physical properties [23,24]. In addition, HP has advantages of simple procedure, rapid reaction and suppressing phase separation (clean phase), surmounting the conventional methods [25]. This clean and rapid HP technology has been applied to obtain pure and homogeneous energy conversion materials [26], which provides an ideal platform to develop catalysts with homogeneous structures.

Herein, we report the fast and clean synthesis and preferred selections of guest 3*d* transition metals (Mn, Co, and Ni)-doped Fe_3C@ carbon nano-onions and electrocatalytic optimization. Co-doped Fe_3C@ carbon nano-onions (FCC@CNOs) with sphere-like core-shell nanostructure morphology is found to exhibit an excellent catalytic performance (η_{10} = 271 mV) and long-term stability in 1.0 M KOH. Realistic structural modelling of the evenly-doped nano-composites was performed by DFT calculations. It indicates that Co doping enhances FCC@CNOs conductivity and the formation of surface Co sites accounts for the enhanced OER activity for FCC@CNOs. The findings provide future prospects and enrich the high-pressure applications in discovery of new catalysts.

2. Experimental section

2.1. Materials and catalyst preparation

The carbon nano-onions (CNOs) were obtained by annealing nanodiamond powder in a tube furnace (ZT-25-20 type). Specifically, the nano-diamond powder (an average size of 5 nm) were annealed at 1500 °C with a heating speed of 10 °C min^{-1}, kept for 30 min in vacuum of ~ 10^{-2} Pa, and then cooled down to the room temperature naturally.

M-doped Fe_3C@CNOs (M = Mn, Co, and Ni) homogeneous phase (abbreviated as FMC@CNOs, FCC@CNOs and FNC@CNOs) were synthesized by a one-step annealing process in cubic multi-anvil press (CS − 1B type, Guilin, China) [27,28]. Firstly, commercial transition-metal powders (Alfa Aesar, ~30 nm) and CNOs (Fe/M/CNOs, 10% M) were mixed in molar ratio of 0.9:0.1:1, and ground for 30 min in the agate mortar (A, Ø 80 mm). Then, the mixtures were prepressed into cylindrical block (Ø 6.8 mm × 3 mm) within a carbide mould at 20 MPa, and encapsulated into *h*-BN capsules in glove box (Ar atmosphere, O_2&H_2O < 0.1 ppm). The samples were annealed at 800 °C for 15 min under 5.0 GPa with graphite heater, and after heating, the cylindrical blocks were quickly cooling to room temperature by circulating water. Finally, the products were peeled out from the assembly, and ultrasonically washed several times with ethanol. For comparison, Fe_3C@CNOs and *x* Co-Fe_3C@CNOs (*x* = 5% and 15%) were also synthesized for comparison at the same conditions.

2.2. Structure characterizations

The crystal structure was checked by X-ray diffraction (XRD, DMAX-2500, Japan) with Cu K*α* radiation source (λ =1.5406 Å, 40 kV, 200 mA) at a scan rate of 2° min^{-1}. The microstructure of Fe_3C@CNOs and M-doped Fe_3C@CNOs (M = Mn, Co and Ni) were investigated by Field Emission Scanning Electron Microscope (FE-SEM, S4800, Japan) and Transmission Electron Microscopy (TEM&HRTEM, JEOL2010, Japan), equipped with Energy Dispersive Spectrometer (EDS). The surface and elemental qualitative analysis were characterized by X-ray Photoelectron Spectroscopy (XPS, AXIS Ultra DLD, Japan) with a monochromatic Al K*α* X-ray source, and all binding energies were referenced to C 1*s* peak (its binding energy set at 284.6 eV). XAS spectra were collected at room temperature using Hard X-ray Micro-Analysis (HXMA) beamline Light Source in Canadian (CLS) and BL15U1 at Shanghai Synchrotron Radiation Facility (SSRF). All measurements were performed in transmission mode using two ion chambers, and computer program IFEFFIT was used to analyze the XANES data [29], according to Co (7709 eV) and Fe (7112 eV) measured for energy calibration. The Raman spectra were recorded by Confocal Raman Microscope (DXR, Thermo − Fisher Scientific) with an excitation line of 532 nm produced from an argon − ion laser. The adsorption-desorption measurements were operated at 77 K by using Brunauer-Emmett-Teller (BET) and Barrett-Joyner-Halenda (BJH) methods (Micromeritics ASAP 2020 V4.04 J).

2.3. Electrochemical measurements

All the cyclic voltammograms were recorded on a CHI 760e electrochemical workstation (Chenhua, Shanghai) in a standard three-electrode system. A glassy carbon (GC) electrode (AFE5050GC, Ø 5 mm) and Ni foam served as working electrode. Hg/HgO (3.5 mol L^{-1} KCl solution) and Pt foil were used as the reference electrode (RE) and the counter electrodes (CE), respectively. The electrode ink was made with 5 mg of the catalyst dispersed into 1 mL of alcohol/water (1:3) mixture containing 35 μ L of Nafion (5 wt%) via ultrasonically treatment for 40 min. 10 μL of ink was deposited on the working electrode. OER polarization curves were obtained in N_2-saturated 1.0 M KOH solution at a scan rate of 2 mV s^{-1}. All electrochemical data were measured versus Hg/HgO without iR compensation according to the following equations [30].

All potentials were converted to the reversible hydrogen electrode (RHE) by the equation of

$$E_{RHE} = E_{Hg/HgO} + 0.098 + 0.059 \times pH \quad (A1)$$

Turnover frequency (*TOF*) was obtained from the equation of

$$TOF = \frac{J}{4Fn} \quad (A2)$$

Where, *J* is current density (η = 0.40 V), *F* is Faraday constant of 96485 C mol^{-1}, and *n* is the moles unit area of electrocatalysts.

The mass activity (*MA*) is calculated at loading of 0.255 mg cm^{-2} by the equation of

$$MA = \frac{A}{M} \tag{A3}$$

Where, A is the current measured (mA), and M is the load amount (mg).

The Faradaic efficiency (*FE*) was calculated as following.

$$FE = \frac{I_R}{I_D N} \tag{A4}$$

Where, I_R and I_D are current obtained by rotating disk electrode at potential of 0.4 V (*vs.* RHE), and *N* is current collection efficiency.

Electrochemical impedance spectroscopy (EIS) measurements were carried out at an overpotential of 320 mV by applying a voltage with an amplitude of 5 mV in a frequency range from 100 kHz to 0.01 Hz. Chronoamperometric (overpotential ($\eta_{10/100}$) of 270/400 mV) testing was employed to investigate the long-term stability of catalysts.

2.4. Computational details

OER reactions over the (210) surface of the pure and Co-doped cementite were modelled using a slab structural model. The cementite slab with a (210) surface was cleaved from the crystal structure, with a thickness of ~7 Å and a vacuum of 15 Å. First-principles calculations were carried out using the 2 × 1 × 1 supercell of the slab cell. The 2 × 1 × 1 supercell for the pure cementite (210) slab has a formula of $(Fe_3C)_{24}$. Single Co dopant was used to replace a Fe atom at surface and interior positions of the pure cementite slab to yield several mono-Co-doped cementite slabs. The geometry optimization and electronic structure calculations for the slab systems were performed using spin-polarized density functional theory (DFT) with Perdew-Burke-Ernzerh (PBE) of exchange correlation functional [31]. The projector augmented wave pseudopotentials were used for describing electron-ion interactions. To test the feasibility of the PBE functional, the bulk cementite was firstly modelled with the Brillouin zone integration performed using a 4 × 4 × 4 Monkhorst-Pack grid, and resultant lattice parameters are in good agreement with the experimental values and the electronic structure is consistent with the prior DFT study (Table S1 and Fig. S1). For the slab simulation, the cutoff energy of the plane wave expansion was set to 500 eV and the Brillouin zone integration was performed using a 4 × 4 × 1 Monkhorst-Pack grid. The active species for the elementary steps of the OER reactions were constructed by adding OER-related adsorbates onto a surface Fe or Co atom of the pure and doped slabs. All the slab structures were optimized using a conjugate-gradient algorithm, during which the energy and force convergence criterions were set to 10^{-4} eV and 0.05 eV $Å^{-1}$, respectively. The phonon dispersion calculations were performed with the optimized structures to evaluate the zero-point-energy corrections used in the calculations of the reaction Gibbs free energies. All the first-principles calculations were carried out using Vienna ab Initio Simulation Package (VASP) [32,33]. The Gibbs free energy changes, ΔG_I to ΔG_V, at the DFT level for the elementary steps I to V over the cementite systems were calculated based on the 4-electron (or 4-hole) mechanism proposed by Norskov for water oxidation [34,35] (Fig. 1).

$$\text{Step I: } OH^- + * \rightarrow * OH + e^- \tag{B1}$$

$$\text{Step II: } * OH^- \rightarrow * O + H^+ + e^- \tag{B2}$$

$$\text{Step III: } OH^- + * O \rightarrow * OOH + e^- \tag{B3}$$

$$\text{Step IV: } * OOH \rightarrow * O_2 + H^+ + e^- \tag{B4}$$

$$\text{Step V: } * O_2 \rightarrow * + O_2 \tag{B5}$$

Where, *X denotes species X adsorbed at a surface active site of cementite. Gibbs free energy changes were obtained by correcting the reaction energies with calculated zero-point-energy and experimental entropy corrections [36]. It is difficult to accurately determine the Gibbs free energy of O_2 with plane wave DFT methods and hence its free energy has been evaluated from the Gibbs free energy change of the reaction

$$2H_2 + O_2 \rightarrow 2H_2O \tag{B6}$$

which is experimentally determined to be 4.92 eV [37,38].

3. Results and discussion

M-doped Fe_3C@CNOs (M = Mn, Co, and Ni) were fabricated via a one-step annealing process under high pressure (Fig. 2). Carbon nano-onions (CNOs) were chosen as an ideal carbon source for the synthesis of metal carbides (TMCs) due to the onion-like concentric graphitic shells with high electrical conductivity (71.8 μS), excellent chemical activity, and large surface area [39,40]. 3*d* transition metals (M = Fe, Mn, Co, and Ni) and CNOs were mixed with stoichiometric ratio in a glovebox (Ar atmosphere) followed by high-pressure annealing, and TMCs were obtained at 800 °C within 15 min under 5.0 GPa. XRD patterns of FCC@CNOs and Fe_3C@CNOs show the strong peaks at 35.2°, 37.7°, 39.8°, 40.6°, 42.9°, 43.8°, 44.6°,45.0°, 45.9°, 48.6°, 49.1°, 51.8°, 54.4°, 56.0° and 58.0°, corresponding to (200), (210), (002), (201), (211), (102), (220), (031), (112), (131), (221), (122), (040), (212) and (301) planes, matching well with the standard patterns of Fe_3C (JCPDS#72-1110) (Fig. 2a). The diffraction peak at 43.9° is indexed to be (211) crystal plane of Fe_3C, which is slightly shifted to higher angle for FCC@CNOs (Inset of Fig. 2a). The lattice distortion is due to the replacement of Fe atoms (R (Fe^{2+}) = 0.76 nm) by Co atoms (R (Co^{2+}) = 0.74 nm). When Co content is increased to 15% or more, the presence of excess impurity peak is observed in the XRD patterns (Fig. S2a), and Fig. S2b shows FCC@CNOs with 10% Co exhibits better OER compared with other contents of Co, therefore we selected 10% metals (M: Fe = 9: 1) doping in this study. Moreover, XRD patterns of FMC@CNOs and FNC@CNOs are also consistent with that of Fe_3C (Fig. S2c). These results suggest that the doping of Mn, Co and Ni atoms do not change the crystal symmetry, and the as-prepared materials have highly crystalline and homogeneous structure.

The morphology of obtained carbides is studied by scanning electron microscopy (SEM) in Fig. 2b and S3b–d, showing a fleecy and porous morphology. Transmission electron microscopy (TEM) images in Fig. 2c reveal that the porous morphology of FCC@CNOs is consisted of a typical sphere-like nanostructure within the size of 100 nm. The high-resolution TEM (HRTEM) images (Fig. 2d) show the clear lattice fringes of 0.24 nm [41], corresponding to the (210) crystal plane of Fe_3C. The crystallization of the particles is further confirmed by the selected area diffraction patterns (Inset of Fig. 2d). Meanwhile, FCC@CNOs is found to exhibit a core-shell structure, closely wrapped by a quasi-spherical CNOs with several concentric graphitic shells [42,43]. The lattice spacing of 0.35 nm for CNOs shells are originated from (002) of graphite [44]. According to the semi-quantitative analysis using EDS-SEM (Table S2 and Fig. S3f), the atomic ratio of Fe:Co in FCC@CNOs is found to be 40.4:4.4, in good agreement with the designed stoichiometric ratio of 9:1 (10% Co). TEM&HRTEM and EDS elemental mappings (Fig. 2e) further illustrate the even distribution of Co, Fe, and C in the homogeneous FCC@CNOs (Fig. S3f), which is benefited from the advantages of high pressure.

N_2 adsorption/desorption isotherm of FCC@CNOs shows a type IV shape with distinct hysteresis loop, confirming the mesoporous character of the material (Fig. 2f). A pore size distribution centered at 8.99 nm is found for FCC@CNOs (Inset of Fig. 2f) [45]. The Brunauer-Emmett-Teller (BET) surface area of FCC@CNOs is calculated to be 112.75 $m^2 g^{-1}$, which is higher than those of reported carbide composites [46,47]. Fe_3C@CNOs also exhibits a hysteresis sorption isotherm curve with average pore size of 8.87 nm with BET surface area of 100.51 $m^2 g^{-1}$ (Fig. S4a). The typical sphere-like nanostructure of FCC@CNOs leads to its high BET surface area, and mesoporous morphology can provide large electrode-electrolyte interfaces and the developed transportation channels for the reaction species [48]. A Raman spectrometer equipped with a 532 nm laser was used to monitor the

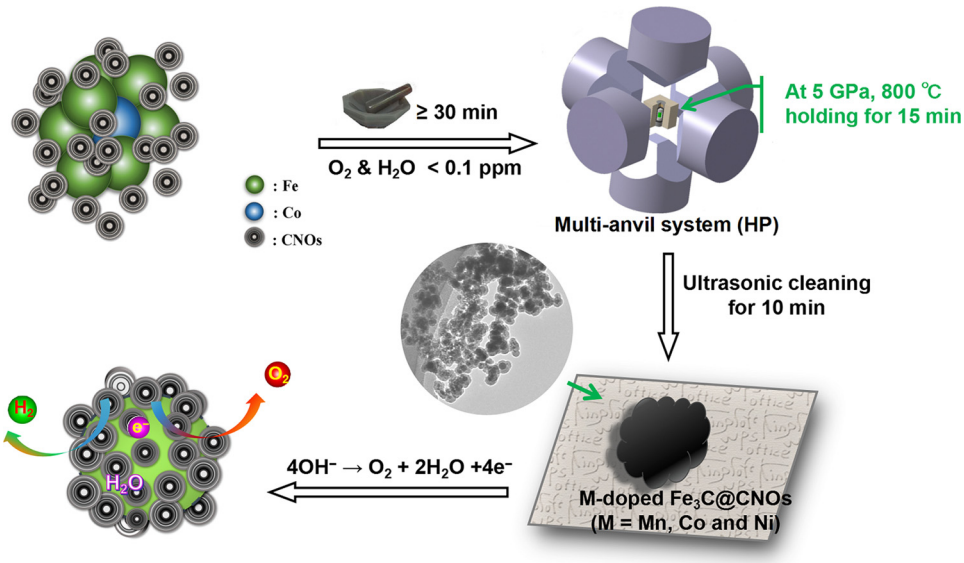

Fig. 1. Schematic illustration for the synthetic process of the M-doped Fe_3C@CNOs (M = Mn, Co and Ni).

graphitization of catalysts. The D-band (I_D = 1342 cm^{-1}) represents the formation of defects in the graphitic lattice, and G-band (I_G = 1584 cm^{-1}) shows the in-plane vibration of sp^2 bonded pairs [49]. Fig. S4b shows that I_D/I_G values are 0.942 for Fe_3C@CNOs and 0.941 for FCC@CNOs, respectively. FCC@CNOs and Fe_3C@CNOs have similar I_D/I_G values, illustrating that Co doping has only small effects on CNOs chemical states. In addition, compared with recently reported Fe/Fe_3C@NGL-NCNT (1.21) and Fe_3C@NCNF-900 (1.25) [50,51], the higher degree of graphitization of FCC@CNOs is beneficial for the electrical conductivity.

X-ray photoelectron spectroscopy (XPS) measurement was conducted to characterize the electronic states. The XPS survey shows the presence of Fe, C and O elements in all samples, while the presence of Co atoms only in FCC@CNOs (Fig. S5a and b). The O element was found from the superficial adsorption due to the exposure to air. The high-resolution spectrum of Co $2p_{3/2}$ (Fig. 2g) can be deconvoluted into three peaks for Co^{2+} $2p_{3/2}$ (780.7 and 786.1 eV) and Co^{3+} $2p_{3/2}$ (782.9 eV) [52,53]. The binding energy (BE) at 284.6 eV is attributed to graphitic carbon (Fig. S5c and d) [49]. As also suggested from Fig. 2d, the disappearance of BE peak at 707.2 eV (Fig. S8a), assigned to Fe-C bond in carbide, is attributed to carbides covered by onion-like carbon shells, which is expected to improve the conductivity and stability of catalysts [54], and the details are discussed later.

The electrocatalytic activities of M-doped Fe_3C@CNOs (M = Co, Mn and Ni) are studied by a standard three-electrode system in 1.0 M KOH solution. As revealed by the linear sweep voltammetry (LSV) curves (Fig. 3a), FCC@CNOs/GC shows a better OER catalytic performance with an overpotential of 320 mV at 10 mA cm^{-2} (η_{10} of 320 mV) than Fe_3C@CNOs/GC (η_{10} of 451 mV), FNC@CNOs /GC (η_{10} of 342 mV), FMC@CNOs/GC (η_{10} of 431 mV) and commercial IrO_2/GC (η_{10} of 350 mV). When deposited on Ni foam, OER activity of FCC@CNOs are further enhanced (Fig. 3b), and the overpotentials of all the hybrids at 10 mA cm^{-2} are shown for a comparison in Fig. 3c. FCC@CNOs/NF exhibits an ideal catalytic performance with only η_{10} of 271 mV, which is much better than those of Fe_3C@CNOs/NF (η_{10} of 345 mV) and RuO_2/NF (η_{10} of 322 mV). Polarization curves of FCC@CNOs obtained with carbon cloth and Ni foam electrode have slight difference (Fig. S2b), indicating the activity of FCC coated on NF is relatively precise. FCC@CNOs/NF also demonstrates an excellent activity compared with recently reported 3*d* transition metal-based catalysts listed in Table S3.

The catalytic kinetics were evaluated by Tafel plots. As revealed in Fig. 3d and S6a, Tafel slope of FCC@CNOs/NF (48.9 mV dec^{-1}) is much smaller than that of Fe_3C@CNOs/NF (89.2 mV dec^{-1}), RuO_2/NF (83.1 mV dec^{-1}), FNC@CNOs (62 mV dec^{-1}) and FMC@CNOs (99 mV dec^{-1}), confirming the favorable kinetics toward OER. Electrochemical impedance spectroscopy (EIS) were collected to understand the electrochemical properties, for which a smaller semicircle indicates a lower resistance value (R_{ct}) and thus a faster charge transfer rate. The semicircle diameter of the FCC@CNOs (32.6 Ω) is much smaller than those of Fe_3C@CNOs (376.5 Ω), FMC@CNOs (151.5 Ω) and FNC@CNOs (43.9 Ω) (Fig. S6b), indicating a lower charge-transfer resistance with rapid electron transfer in the FCC@CNOs electrode. EIS results confirm that doping of Co atoms can enhance the electron conductivity of Fe_3C, which counts in the acceleration of OER kinetics [55].

Electrochemically active surface areas (ECSAs) were evaluated by the electrochemical double-layer capacitance (C_{dl}) [56], and CV plots were collected between 0.1 and 0.2 V at different scan rate in 1.0 M KOH (Fig. S6c–S6f). FCC@CNOs presents a capacitance of 99.18 m F cm^{-2} nearly 5 times of that of Fe_3C@CNOs (20.78 m F cm^{-2}) (Fig. 3e), indicating that the specific morphology of FCC@CNOs provides a larger active surface area. The turnover frequency (TOF) and massive activity (MA) were shown in Fig. 3e and S7a, the FCC@CNOs (0.212/0.08 s^{-1}) has a lager TOF value than those of Fe_3C@CNOs (0.052/0.003 s^{-1}), FNC@CNOs (0.06 s^{-1}) and FMC@CNOs (0.01 s^{-1}), while FCC@CNOs has higher MA value (39.22 A g^{-1}) than the others. In addition, the high Faradaic efficiency (> 90%) indicated that the reaction on the disk electrode was mainly OER, rather than the oxidation of catalysts in Fig. S7b, suggesting the excellent intrinsic activity of FCC@CNOs [30].

Moreover, FCC@CNOs exhibits a long-term stability with 97% retention for more than 40 h at 100/10 mA cm^{-2} (400/270 mV) in Fig. 3f. After 10000 CV cycles, the polarization curves have the negligible changes (Fig. S7c), which might be resulted from the surface reconstruction or the weak mechanical binding between FCC@CNOs powder and Ni foam carrier [57]. Additionally, the main XRD pattern of collected sample after OER still matches well with Fe_3C-type structure (JCPDS#72-1110) (Fig. S7d) and I_D/I_G of FCC@CNOs has almost no change (Fig. S4a), confirming structural stability of FCC@CNOs, which facilitates a superior catalytic stability.

The coordination environment and chemical states of FCC@CNOs after OER were investigated by XPS combined with before. The Fe 2*p* peaks of 710.7 eV, 715.9 eV and 724.9 eV are assigned to Fe^{2+}, and the peaks at 713.1 eV and 719.3 eV (satellite peak) are attributed to Fe^{3+} in Fe_3C@CNOs [58]. When Co atom is doped into Fe_3C@CNOs, the ratio at 713.1 eV (Fe^{3+} $2p_{3/2}$) and 710.7 eV (Fe^{2+} $2p_{3/2}$) (abbreviated to Fe^{3+}/Fe^{2+}) increases to 1.00 from initial 0.80 (Fig. S8a). While Co in FCC@CNOs has a low valance state with high Co^{3+}/Co^{2+} ratio of 0.6,

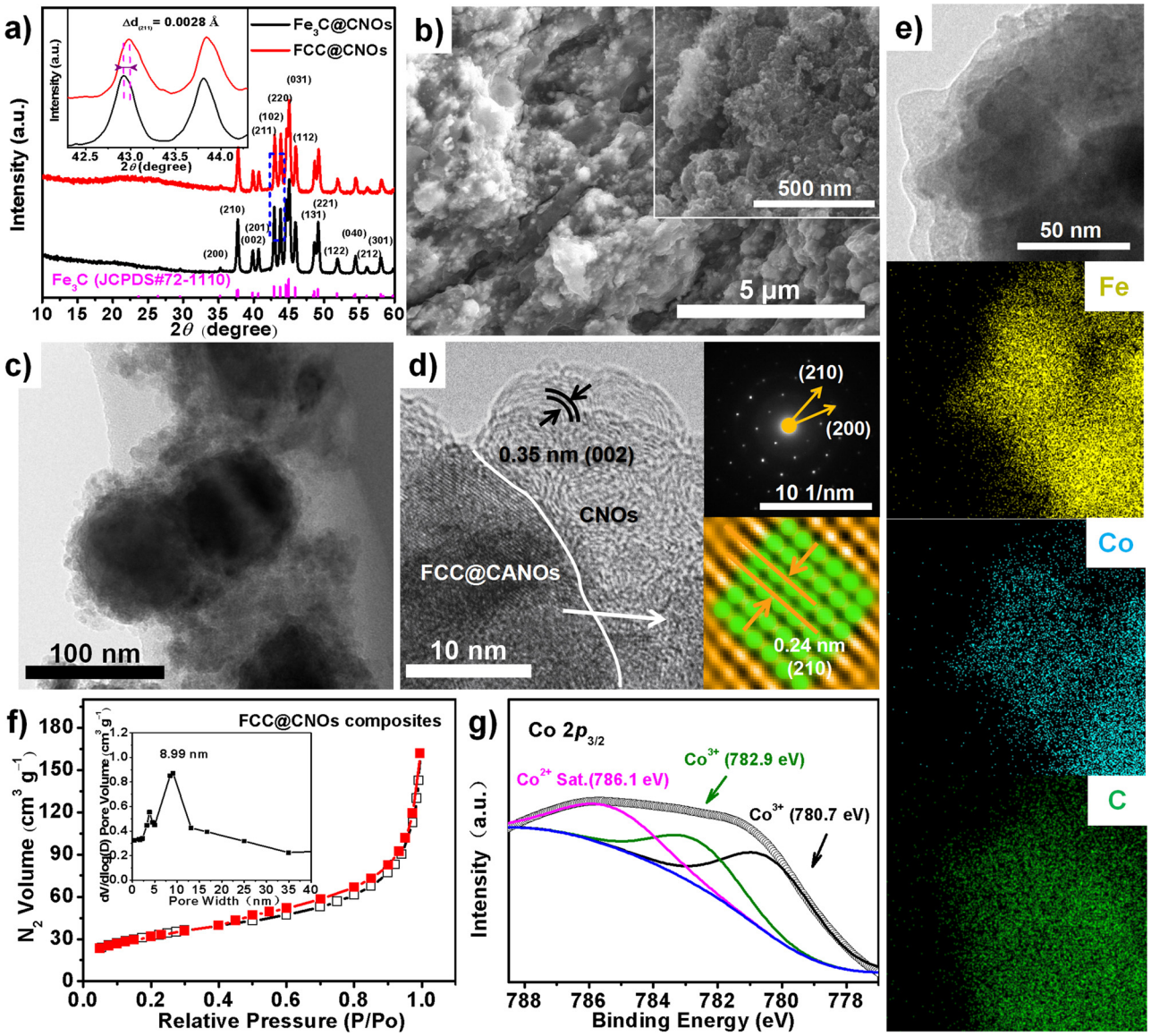

Fig. 2. Characterizations of the structure and morphology of FCC@CNOs. a) XRD diffraction patterns, b) SEM (inset of magnification), c) TEM, d) HRTEM images and diffraction pattern (inset) and e) EDS mapping scans of FCC@CNOs. f) N_2 adsorption/desorption isotherm of FCC@CNOs and the corresponding pore size distribution (inset image) in the high pressure region (P/P_o = 0.4–1) and g) Co $2p_{3/2}$ spectrum of FCC@CNOs.

indicating the strong interaction of Fe and Co atoms. During OER process, the ratio of Fe^{3+}/Fe^{2+} (713.1 eV/710.8 eV) increases to 1.1 from 1.0, while the ratio of Co^{3+}/Co^{2+} (782.9 eV/780.7 eV) visibly increases to 1.6 from 0.6 compared with FCC@CNOs before (Fig. 4a and b) [59,60], suggesting that both Fe atom and Co atom on the surface are oxidized to high valence state improving ability of OER. In additional, the peak located at 530.0 eV is associated with the oxygen bonded to the transition metals, such as Fe-O and Co-O [49], and the peak at 533.0 is assigned to O species (O*, OH* or OOH*) (Fig. S8b) [52,53]. Co doping causes the peak at 533.0 eV shifting to a higher value (533.6 eV), suggesting that chemisorbed oxygen and the low-coordinated oxygen ions formed on the surface. After OER, O 1*s* spectrum of FCC@CNOs at 530.0 eV is positively shifted by 0.6 eV, corresponding to high oxidation state of metals, and the peak at 531.9 eV is positively shifted by 0.4 eV, indicating that catalysts are more easily oxidized to high chemical valence to form the O species-rich (O*, OH* or OOH*) surface. The peak of O 1*s* is significantly enhanced and a new peak located at 535.6 eV is related to chemisorbed OH* formed on the surface (Fig. S8b). Therefore, the introduction of Co atom promotes the electronic structure adjustment of FCC@CNOs on the surface, and the synergistic effect of highly active Co atom with Fe atom is conducive to the adsorption of oxy(hydroxyl), which improves OER activity greatly.

XAS characterizations were further employed to elucidate the atomic structure of FCC@CNOs before and after OER. Co K-edge absorption position of FCC@CNOs catalyst (7727.5 eV) is found in the region between CoO (7725.2 eV) and Co_2O_3 (7730.5 eV) (Fig. 4c), while the Fe K-edge spectra for FCC@CNOs catalyst (7130.5 eV) is located between that of FeO (7129.0 eV) and FeOOH (7132 eV) (Fig. 4d) [61,62]. Therefore, the oxidation state of Co atom and Fe atom in FCC@CNOs is suggested to be between M^{2+} and M^{3+} [63], and Fe absorption K-edge was shifted to high energy after Co doping in Fig. S9a, suggesting the electron density depletion of the surface Fe, agreeing with our XPS results. Co K-edge of EXAFS spectrum for FCC@CNOs catalyst shows a dominant peak at 1.9 Å associated with the back scattering of Co-C in the first shell (Fig. 4e), and the structure parameters of Co atom have been extracted from the EXAFS fitting in Table S4, indicating that Co atoms enter into the Fe_3C lattices. After OER, the normalized XANES spectra show that the main absorption peaks for Co and Fe K-edge have drifted toward higher energy by 1.5 eV and 0.2 eV, respectively (Fig. S9a and S9b), indicating that Co atom

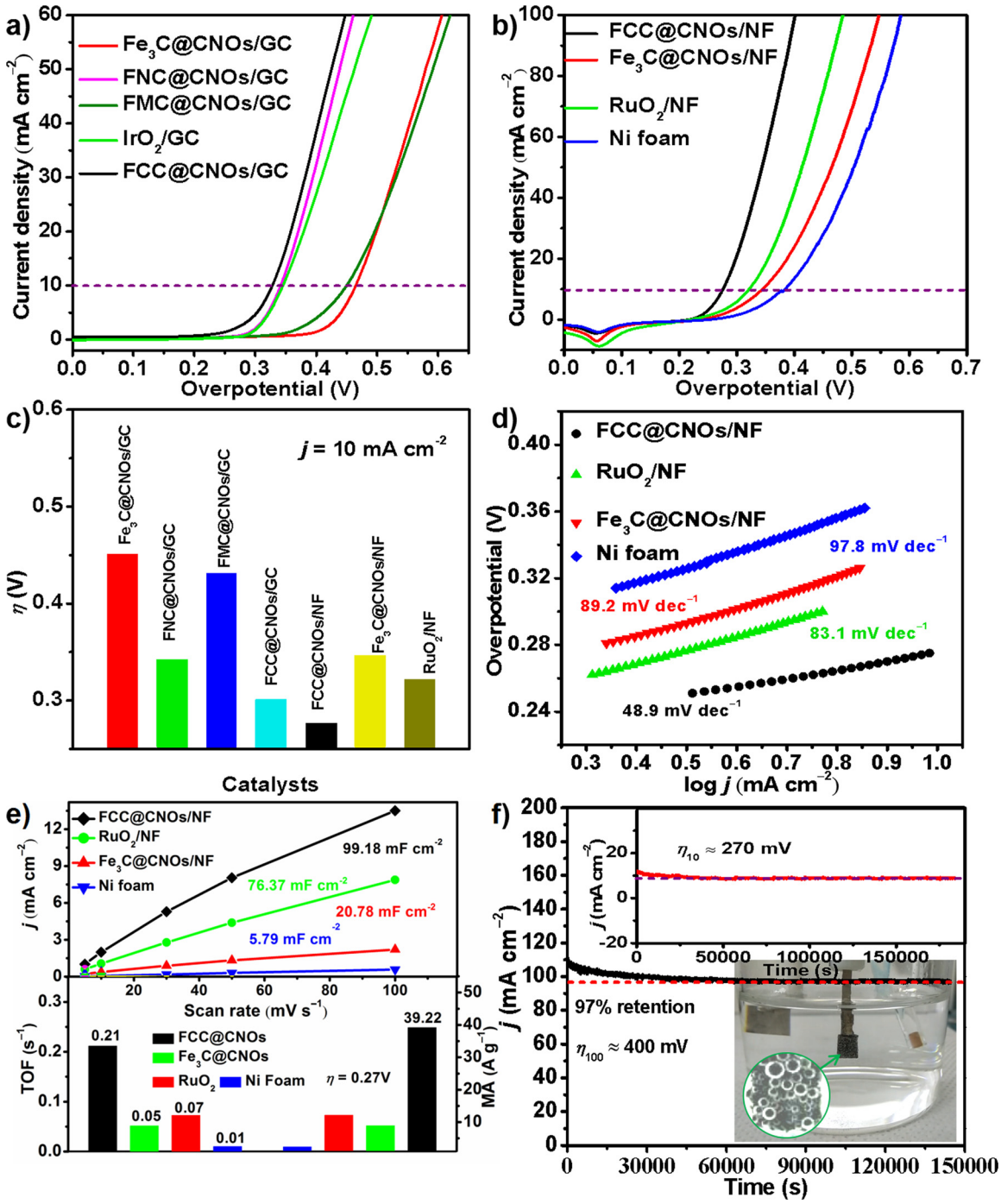

Fig. 3. LSV curves of M-doped Fe_3C@CNOs (M = Mn, Co, and Ni) and Fe_3C@CNOs measured on a) glassy carbon (GC) and b) Ni foam for OER at 5 mV s^{-1} in 1.0 M KOH. c) Comparison of the overpotential required at 10 mA cm^{-2} for different catalysts. d) Tafel plots obtained with FCC@CNOs, Fe_3C@CNOs, RuO_2 and Ni foam. e) The current density versus scan rate, TOF and MA values of different catalysts. f) Chronoamperometric testing of FCC@CNOs/Ni foam at overpotential of about 400 and 270 mV (100/10 mA cm^{-2}), and the inset image shows catalytic electrolytic cell.

carries more positive change than Fe atom. In addition, EXAFS analysis shows the bond length of Co-C (1.9 Å) is shortened to 1.8 Å in Fig. 4e, and Fe K-edge EXAFS spectrum reveals the slight shortening of Fe-C bond length in Fig. 4f, in line with higher oxidation state with smaller cation radius [64]. The XANES and EXAFS analysis are consistent with XPS results. The interaction of Fe and Co regulates the electronic structure of FCC@CNOs and surface-doped Co atom has more highly activity than Fe atom.

To further explain the origins of the different OER performances, first-principles calculations were employed. According to HRTEM analysis, OER over the (210) surfaces of the pristine and Co-doped cementite were modelled at the DFT level with PBE functional. The OER performance of pure and doped cementite systems can be predicted using Gibbs free energy(ΔG) profiles for the elementary OER steps (steps I to V in Fig. 5a). The proposed OER mechanism involves $4h^+$, which is detailed in computational details [65]. Firstly, *OH is formed by OH^- adsorbing at the surface of the catalyst when combining with an h^+, which can further lose H^+ to form *O species aided by a second h^+. Then, *O can bind with OH^- to form *OOH with a third h^+. The *OH, *O and *OOH are the key intermediates in the OER

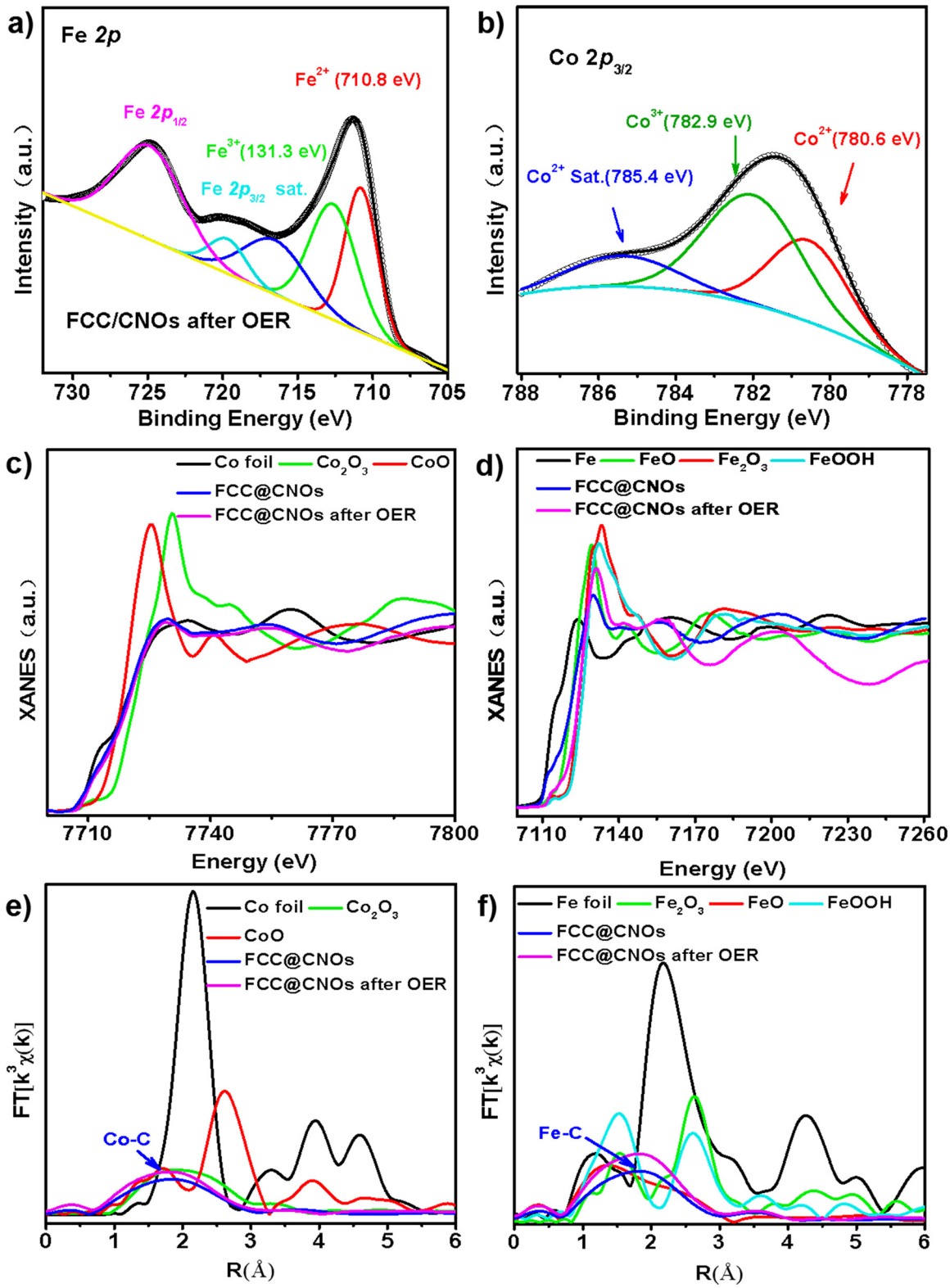

Fig. 4. XPS and XAS analysis of FCC@CNOs. a) Fe 2*p* and b) Co 2*p* of FCC@CNOs after OER process. All fitted peaks of as-prepared and "Sat." indicates satellite peaks. Normalized c) Co and d) Fe K-edge XANES spectra of FCC@CNOs, FCC@CNOs after OER and references. Magnitude of transformed EXAFS spectra of e) Co and f) Fe edge for FCC@CNOs, FCC@CNOs after OER and references.

process. Finally, OOH species can combine with OH^- to release O_2 with a fourth h^+.

We first compare the activation energy over the surface Fe sites of the pure and mono-Co-doped cementite systems. Four mono-Co-doped cementite systems are constructed (Fig. S10), in which the selected surface Fe site is coordinated to a Co at different positions. The elementary steps involve surface species for the OER over a surface Fe of cementite in Fig. S11. Comparable OER free energy profiles are obtained for the four mono-Co-doped and the pure cementite systems (Fig. S12), with step III being the rate-limiting step ($\Delta G_{III} \approx 2.8$ eV). This

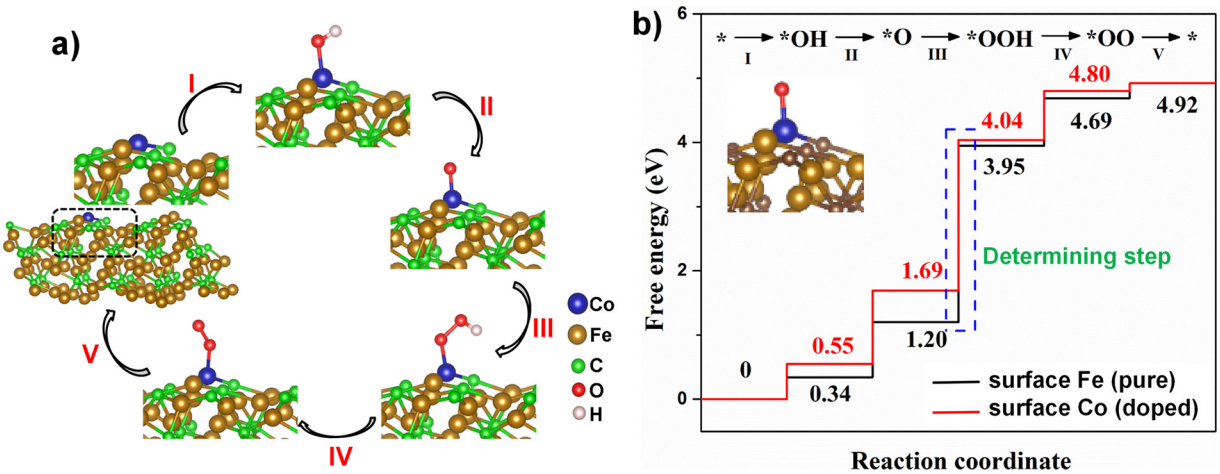

Fig. 5. a) OER species adsorbed at a Co-site on (210) surface of Co-doped cementite, b) Gibbs free energy profile for OER over a Fe site of pure cementite (black line) and over a Co site of Co-doped cementite (red line) (For interpretation of the references to colour in this figure legend, the reader is referred to the web version of this article).

implies that the influence of forming Co-Fe dimer upon Co doping on the catalytic performance of surface Fe is not so significant. However, the experimental results show that Co-doped cementite has much lower OER overpotential than pure cementite. Since Co doping cannot significantly improve the catalytic mechanism of the surface Fe, it may be possible that Co dopant not only acts like a co-catalyst but also a catalytic site by itself. To verify out our hypothesis, the OER free energy profiles for a surface Fe and a surface Co at the same lattice position of cementite (Fe in pure cementite and Co in Co-doped cementite) are calculated and compared, as shown in Fig. 5b. The Gibbs free energy change for the rate-limiting step, ΔG_{III}, is 2.35 eV for the Co-catalyzed OER, 0.40 eV lower than ΔG_{III} (2.75 eV) for the Fe-catalyzed OER (Fig. 5b), which suggests the Co-catalyzed OER requires a lower external bias potential. This is mainly due to the different adsorption strengths of the OER species at Co and Fe (the difference in adsorption strengths of an OER species at Co and Fe equals the difference in the heights of the corresponding plateau in the free energy profiles for the Co and Fe). Adsorption and interconversion of OER species will change the oxidation state of the metal catalyst site. When forming adsorption with OER species such as *OH and *O, the unreacted surface metal site with an oxidation state of M^{1+} will be oxidized. For example, step I is to oxidize M^{1+} to M^{2+} and step II is to convert M^{2+} to M^{3+}. The conversion from M^{1+} to M^{2+} can be related to the second ionization potential (IP_{II} = $E(M^{1+})$ – $E(M^{2+})$) of M, whereas the M^{2+} to M^{3+} conversioncan be related to the third ionization potential (IP_{III} = $E(M^{2+})$ – $E(M^{3+})$) of M. Higher IP indicates metal being more difficult to oxidize. In our case, IP_{II} (Co) is slightly higher than IP_{II} (Fe) (17.08 eV vs 16.20 eV) [66,67], explaining that ΔG_I(Co) is slightly higher than ΔG_{II}(Fe) in Fig. 5b. IP_{III} (Co) is much higher than IP $_{III}$ (Fe) (33.50 eV vs 30.65 eV) [68], which is mainly responsible for the much lower barrier for the rate-limiting reaction step over Co (ΔG_{III} (Co)) than that over Fe (ΔG_{III} (Fe)). Therefore, the OER enhancement by surface Co is in part due to its suitable susceptibility to oxidation. The resultant comparatively evenly spaced OER steps over the Co site may account for the remarkably low overpotential for FCC@CNOs. Similarly, the OER free energy profiles for the Ni- and Mn-doped cementite systems are predicted (Fig. S13). The surface Mn site from Mn-doping shows worse OER activity than the surface Fe site. Ni-doping enhances the OER activity of cementite; and according to the predicted rate-limiting barrier (ΔG_{III}), the enhancement effects are slightly greater than those by Co doping. It is also noted that ΔG for OER initiation (* → *OH) with Co is smaller than Ni, The results are qualitatively in line with experimental ordering of OER performances with Co ≈ Ni > Fe > Mn, and are also consistent with trend in IP(II) (Ni:18.17 > Co:17.08 > Fe:16.20 > Mn: 15.64 eV) as well as the metal oxidation states in stable common oxides (Mn: + 4 > Fe: + 2/ + 3 = Co: + 2/ + 3 > Ni: + 2). Based on the comparison of the OER profiles by the pure and doped cementite systems, it is suggested that surface Fe of cementite forms too strong adsorption in *O to achieve theoretically low overpotential, and dopants that bring about weaker adsorption in *O might result in enhancement in OER performance. In the current study, the Co- and Ni-doping introduce new surface catalytic sites that exhibit frustrated high oxidation states, which might be the key to optimizing the OER performance of the cementite materials.

DFT results also suggest that Co doping enhances the conductivity of the cementite material. The computational model for FCC was built by replacing 1 out of 12 Fe atoms by Co atom in a $(Fe_3C)_4$ super-cell, which is very close to the 10% doping ratio in the experiments, and the densities of states (DOSs) were calculated for the pure and doped bulk crystal. It could be easily implied that Fe_3C shows metallic behavior because of the non-vanishing DOS value at the Fermi level (Fig. S14a). The DOS states are contributed by Fe atoms near Fermi level, and the contribution of C atoms could be neglected. While for the Co-doped Fe_3C, although only 10% of Fe atoms are replaced by Co, the significant contribution from Co atoms to the valence band near the Fermi level can be observed clearly. The integrated valence band DOS area upon Co doping increases from 1.007 to 1.143 for the spin-up states, and from 1.633 to 2.543 for the spin-down states near the Fermi level, indicating that the participation of Co can indeed enhance the conductivity of FCC@CNOs. The single-atom projected densities of states (PDOSs) of a Fe atom and a Co atom at the same lattice position of cementite (210) slab are shown in Fig. S14b and c. The PDOSs show that both Co and Fe atoms contribute to the metallicity of the cementite materials, but Co, both the surface and interior ones, has a larger electron population in the valence band close to the Fermi level than corresponding Fe does. For the surface Co doping, this effect is more significant, and additional shifting of the valence band peak toward the Fermi level has been observed.

4. Conclusion

In summary, a time-saving, effective high-pressure annealing technique was reported for synthesizing pure and highly crystalline metal-doped Fe_3C@CNOs OER catalysts. Compared to traditional synthetic strategies, M-doped Fe_3C@CNOs (M = Mn, Co and Ni) materials prepared by high pressure have the characteristic of high crystallinity, clean and homogeneous nanostructure, which provide efficient dispersion of active sites and great convenience for the recognition of these

sites. The as-prepared Co-doped Fe_3C@CNOs (FCC@CNOs) exhibits an ideal OER performance, with a low η_{10} of only 271 mV (Tafel slope of 48.9 mV dec^{-1}) and the long-term stability of 40 h (100 mA cm^{-2}). Exceptional electro-catalytic performance of FCC@CNOs is attributed to several factors: (1) mesoporous core-shell nanostructures endow large amount of exposed active sites, efficient mass transfer and catalytic stability; (2) Co doping alters the surface electronic structure, improving conductivity and lowering the kinetic barrier of FCC@CNOs. (3) the formation of surface Co acts as critical active sites forimproved OER activity even at a low doping concentration. Density functional theory calculations show that Co tends to form weaker *O adsorption than Fe does, which leads to a lower reaction barrier for the rate-limiting OER elementary step (*O→*OOH). The study opens a new avenue for the efficient synthesis of high performance electrocatalysts and new understandings for synergistic effect of multiple metals.

Declaration of interest statement

We wish to draw the attention of the Editor to the following facts which may be considered as potential conflicts of interest and to significant financial contributions to this work. We wish to confirm that there are no known conflicts of interest associated with this publication and there has been no significant financial support for this work that could have influenced its outcome. We confirm that the manuscript has been read and approved by all named authors and that there are no other persons who satisfied the criteria for authorship but are not listed. We further confirm that the order of authors listed in the manuscript has been approved by all of us. We confirm that we have given due consideration to the protection of intellectual property associated with this work and that there are no impediments to publication, including the timing of publication, with respect to intellectual property. In so doing we confirm that we have followed the regulations of our institutions concerning intellectual property. We understand that the Corresponding Author is the sole contact for the Editorial process (including Editorial Manager and direct communications with the office). He is responsible for communicating with the other authors about progress. We confirm that we have provided a current, correct email address which is accessible by the Corresponding Author and which has been configured to accept email from *Appl. Catal. B: Environ.*

Declaration of Competing Interest

The authors declare no conflict of interest

Acknowledgements

We thank the financial supports from National Natural Science Foundation of China (U1930402).

Appendix A. Supplementary data

Supplementary material related to this article can be found, in the online version, at doi:https://doi.org/10.1016/j.apcatb.2019.118385.

References

[1] L. Han, S. Dong, E. Wang, Transition-metal (Co, Ni, and Fe)-based electrocatalysts for the water oxidation reaction, Adv. Mater. 28 (2016) 9266–9291.
[2] Roger, M.A. Shipman, M.D. Symes, Earth-abundant catalysts for electrochemical and photoelectrochemical water splitting, Int. Rev. Chem. Eng. 1 (2017) 3.
[3] Q. Shi, C. Zhu, D. Du, Y. Lin, Robust noble metal-based electrocatalysts for oxygen evolution reaction, Chem. Soc. Rev. 48 (2019) 3181–3192.
[4] B. Yang, N. Zhang, G. Chen, K. Liu, J. Yang, A. Pan, M. Liu, X. Liu, R. Ma, T. Qiu, Serpentine $Co_xNi_{3-x}Ge_2O_5(OH)_4$ nanosheets with tuned electronic energy bands for highly efficient oxygen evolution reaction in alkaline and neutral electrolytes, Appl. Catal. B: Environ. 260 (2019) 118184.
[5] F. Song, L. Bai, A. Moysiadou, S. Lee, C. Hu, L. Liardet, X. Hu, Transition metal oxides as electrocatalysts for the oxygen evolution reaction in alkaline solutions: an Application-Inspired renaissance, J. Am. Chem. Soc. 140 (2018) 7748–7759.
[6] Y. Wang, K. Li, F. Yan, C. Li, C. Zhu, X. Zhang, Y. Chen, Integration of Mo_2C-embedded nitrogen-doped carbon with Co encapsulated in nitrogen-doped graphene layers derived from metal-organic-frameworks as multi-functional electrocatalyst, Nanoscale 11 (2019) 12563–12572.
[7] Ya. Liu, X. Luo, C. Zhou, S. Du, D. Zhen, B. Chen, J. Li, Q. Wu, Y. Iru, D. Chen, A modulated electronic state strategy designed to integrate active HER and OER components as hybrid heterostructures for efficient overall water splitting, Appl. Catal. B: Environ. 260 (2019) 118197.
[8] N. Han, K.R. Yang, Z. Lu, Y. Li, W. Xu, T. Gao, Z. Cai, Y. Zhang, V.S. Batista, W. Liu, X. Sun, Nitrogen-doped tungsten carbide nanoarray as an efficient bifunctional electrocatalyst for water splitting in acid, Nat. Comm. 9 (2018) 924.
[9] Y. Zhao, J. Zhang, X. Guo, H. Fan, W. Wu, H. Liu, G. Wang, Fe_3C@nitrogen doped CNT arrays aligned on nitrogen functionalized carbon nanofibers as highly efficient catalysts for the oxygen evolution reaction, J. Mater. Chem. A 5 (2017) 19672–19679.
[10] F. Kong, X. Fan, A. Kong, Z. Zhou, X. Zhang, Y. Shan, Covalent phenanthroline framework derived FeS@Fe_3C composite nanoparticles embedding in N-S-codoped carbons as highly efficient trifunctional electrocatalysts, Adv. Funct. Mater. 28 (2018) 1803973.
[11] Z. Li, Q. Gao, X. Liang, H. Zhang, H. Xiao, P. Xu, Z. Liu, Low content of Fe_3C anchored on Fe, N, S-codoped graphene-like carbon as bifunctional electrocatalyst for oxygen reduction and oxygen evolution reactions, Carbon 150 (2019) 93–100.
[12] H. Fan, H. Yu, Y. Zhang, Y. Zheng, Y. Luo, Z. Dai, B. Li, Y. Zong, Q. Yan, Fe-doped Ni_3C nanodots in N-doped carbon nanosheets for efficient hydrogen-evolution and oxygen-evolution electrocatalysis, Angew. Chem. Int. Ed. 56 (2017) 12566–12570.
[13] Y. Wu, X. Tao, Y. Qing, H. Xu, F. Yang, S. Luo, C. Tian, M. Liu, X. Lu, Cr-doped FeNi-P nanoparticles encapsulated into N-doped carbon nanotube as a robust bifunctional catalyst for efficient overall water splitting, Adv. Mater. 31 (2019) 1900178.
[14] X. Zhong, W. Yi, Y. Qu, L. Zhang, H. Bai, Y. Zhu, J. Wan, S. Chen, M. Yang, L. Huang, M. Gu, H. Pan, B. Xu, Co single-atom anchored on Co_3O_4 and nitrogen-doped active carbon toward bifunctional catalyst for zinc-air batteries, Appl. Catal. B: Environ. 260 (2019) 118188.
[15] J. Xu, J. Li, D. Xiong, B. Zhang, Y. Liu, K. Wu, I. Amorim, W. Li, L. Liu, Trends in activity for the oxygen evolution reaction on transition metal (M = Fe, Co, Ni) phosphide pre-catalysts, Chem. Sci. 9 (2018) 3470–3476.
[16] D. Zhu, Y. Huang, J. Cao, S.C. Lee, M. Chen, Z. Shen, Cobalt nanoparticles encapsulated in porous nitrogen-doped carbon: oxygen activation and efficient catalytic removal of formaldehyde at room temperature, Appl. Catal. B: Environ. 258 (2019) 117981.
[17] B. Zhang, X. Zheng, O. Voznyy, R. Comin, M. Bajdich, M. Garciamelchor, L. Han, J. Xu, M. Liu, L. Zheng, F.P.G. Arquer, C.T. Dinh, F. Fan, E. Yassitepe, N. Chen, T. Regier, P. Liu, Y. Li, P.D. Luna, A. Janmohamed, H.L. Xin, H. Yang, A. Vojvodic, E.H. Sargent, Homogeneously dispersed multimetal oxygen-evolving catalysts, Science 352 (2016) 333–337.
[18] Y. Zhong, X. Xia, F. Shi, J. Zhan, J. Tu, H. Fan, Transition metal carbides and nitrides in energy storage and conversion, Adv. Sci. 3 (2016) 1500286.
[19] H. Wang, F.X. Yin, N. Liu, R.H. Kou, X.B. He, C.J. Sun, B.H. Chen, D.J. Liu, H.Q. Yin, Engineering Fe-Fe_3C@Fe-N-C active sites and hybrid structures from dual metal-organic Frameworks for oxygen reduction reaction in H2-O2 fuel cell and Li-O2 battery, Adv. Funct. Mater. 29 (2019) 1901531.
[20] S. Dutta, A. Indra, H. Han, T. Song, An intriguing pea-like nanostructure of cobalt phosphide on molybdenum carbide incorporated nitrogen-doped carbon nanosheets for efficient electrochemical water splitting, ChemSusChem 11 (2018) 3956–3964.
[21] Q. Jin, Ren B, J. Chen, H. Cui, C. Wang, A facile method to conduct 3D self-supporting Co-FeCo/N-doped graphene-like carbon bifunctional electrocatalysts for flexible solid-state zinc air battery, Appl. Catal. B: Environ. 256 (2019) 117887.
[22] H. Han, K.M. Kim, H. Choi, G. Ali, K.Y. Chung, Y.R. Hong, J. Choi, J. Kwon, S.W. Lee, J.W. Lee, J.H. Ryu, T. Song, S. Mhin, Parallelized reaction pathway and stronger internal band bending by partial oxidation of metal sulfide-graphene composites: important factors of synergistic oxygen evolution reaction enhancement, ACS Catal. 8 (2018) 4091–4102.
[23] J.P.S. Walsh, D.E. Freedman, High-pressure synthesis: a new frontier in the search for next-generation intermetallic compounds, Acc. Chem. Res. 51 (2018) 1315–1323.
[24] L. Zhang, Y. Wang, J. Lv, Y. Ma, Materials discovery at high pressures, Nat. Rev. Mater. 2 (2017) 17005.
[25] H. Sun, X. Jia, L. Deng, P. Lv, X. Guo, Y. Zhang, B. Sun, B. Liu, H. Ma, Effect of HPHT processing on the structure, and thermoelectric properties of Co_4Sb_{12} co-doped with Te and Sn, J. Mater. Chem. A 3 (2015) 4637–4641.
[26] I. Yamada, T. Odake, K. Asai, K. Oka, S. Kawaguchi, K. Wada, S. Yagi, High-pressure synthesis of highly oxidized $Ba_{0.5}Sr_{0.5}Co_{0.8}Fe_{0.2}O_{3-\delta}$ cubic perovskite, Mater. Chem. Front. 3 (2019) 1209–1217.
[27] R.H. Bagramov, V.D. Blank, N.R. Serebryanaya, G.A. Dubitsky, E.V. Tatyanin, V.V. Aksenenkov, High pressures synthesis of iron carbide nanoparticles covered with onion-like carbon shells, Fuller. Nanotub. Car. N. 20 (2012) 41–48.
[28] A. Tsuzuki, S. Sago, S.I. Hirano, S. Naka, High temperature and pressure preparation and properties of iron carbides Fe_7C_3 and Fe_3C, J. Mater. Sci. 19 (1984) 2513–2518.
[29] B. Ravel, M. Newville, ATHENA, ARTEMIS, HEPHAESTUS: data analysis for X-ray absorption spectroscopy using IFEFFIT, J. Synchrotron Radiat. 12 (2005) 537–541.
[30] Y. Hong, S. Mhin, K. Kim, W. Han, H. Choi, G. Ali, K.Y. Chung, H.J. Lee, S.I. Moon, S. Dutta, S. Sun, Y.G. Jung, T. Song, H. Han, Electrochemically activated cobalt nickel sulfide for an efficient oxygen evolution reaction: partial amorphization and phase control, J. Mater. Chem. A 7 (2019) 3592–3602.
[31] J.P. Perdew, K. Burke, M. Ernzerhof, Generalized gradient approximation made

simple, Phys. Rev. Lett. 77 (1996) 3865–3868.
[32] G. Kresse, J. Furthmuller, Efficient iterative schemes for ab initio total-energy calculations using a plane-wave basis set, Phys. Rev. B 54 (1996) 11169–11186.
[33] G. Kresse, J. Furthmuller, Efficiency of ab-initio total energy calculations for metals and semiconductors using a plane-wave basis set, Comp. Mater. Sci. 6 (1996) 15–50.
[34] J. Rossmeisl, A. Logadottir, J.K. Norskov, Electrolysis of water on (oxidized) metal surfaces, Chem. Phys. 319 (2005) 178–184.
[35] J. Rossmeisl, Z.W. Qu, H. Zhu, G.J. Kroes, J.K. Norskov, Electrolysis of water on oxide surfaces, J. Electroanal. Chem. 607 (2007) 83–89.
[36] J.K. Norskov, T. Bligaard, A. Logadottir, J.R. Kitchin, J.G. Chen, S. Pandelov, U. Stimming, Trends in the exchange current for hydrogen evolution, J. Electrochem. Soc. 152 (2005) J23–J26.
[37] J.K. Norskov, J. Rossmeisl, A.A. Logadottir, L. Lindqvist, J.R. Kitchin, T. Bligaard, H. Jonsson, Origin of the overpotential for oxygen reduction at a fuel-cell cathode, J. Phys. Chem. B 108 (2004) 17886–17892.
[38] K. Srinivasu, S.K. Ghosh, Transition metal decorated graphyne: an efficient catalyst for oxygen reduction reaction, J. Phys. Chem. C 117 (2013) 26021–26028.
[39] A. Camisasca, A. Sacco, R. Brescia, S. Giordani, Boron/Nitrogen-codoped carbon nano-onion electrocatalysts for the oxygen reduction reaction, ACS Appl. Nano Mater. 1 (2018) 5763–5773.
[40] O. Mykhailiv, H. Zubyk, M.E. Plonskabrzezinska, Carbon nano-onions: unique carbon nanostructures with fascinating properties and their potential applications, Inorg. Chim. Acta Rev. 468 (2017) 49–66.
[41] Y. Hou, T. Huang, Z. Wen, S. Mao, S. Cui, J. Chen, Metal – organic framework-derived nitrogen-doped core-shell-structured porous Fe/Fe_3C@C nanoboxes supported on graphene sheets for efficient oxygen reduction reactions, Adv. Energy Mater. 4 (2014) 1220–1225.
[42] E. Tovarmartinez, J.A. Morenotorres, J.V. Cabrerasalazar, M. Reyesreyes, L.F. Chazaroruiz, R. Lopezsandoval, Synthesis of carbon nano-onions doped with nitrogen using spray pyrolysis, Carbon 140 (2018) 171–181.
[43] K. Chatterjee, M. Ashokkumar, H. Gullapalli, Y. Gong, R. Vajtai, P. Thanikaivelan, P.M. Ajayan, Nitrogen-rich carbon nano-onions for oxygen reduction reaction, Carbon 130 (2018) 645–651.
[44] H. Tang, X. Yuan, P. Yu, Q. Hu, M. Wang, Y. Yao, L. Wu, Q. Zou, Y. Ke, Y. Zhao, Revealing the formation mechanism of ultrahard nanotwinned diamond from onion carbon, Carbon 129 (2018) 159–167.
[45] Y. Niu, X. Huang, W. Hu, Fe_3C nanoparticle decorated Fe/N doped graphene for efficient oxygen reduction reaction electrocatalysis, J. Power Sour. 332 (2016) 305–311.
[46] Y. Zhang, J. Zai, K. He, X. Qian, Fe_3C nanoparticles encapsulated in highly crystalline porous graphite: salt-template synthesis and enhanced electrocatalytic oxygen evolution activity and stability, Chem. Comm. 54 (2018) 3158–3161.
[47] J. Wang, L. Wang, S. Yang, VN quantum dots anchored uniformly onto nitrogen-doped graphene as efficient electrocatalysts for oxygen reduction reaction, Nano 13 (2018) 1850041.
[48] Y. Han, Y.G. Wang, W. Chen, R. Xu, L. Zheng, J. Zhang, J. Luo, R.A. Shen, Y. Zhu, W.C. Cheong, C. Chen, Q. Peng, D. Wang, Y. Li, Hollow N-doped carbon spheres with isolated cobalt single atomic sites: superior electrocatalysts for oxygen reduction, J. Am. Chem. Soc. 139 (2017) 17269–17272.
[49] M. Ma, S. You, W. Wang, G. Liu, D. Qi, X. Chen, J. Qu, N. Ren, Biomass-derived porous Fe_3C/tungsten carbide/graphitic carbon nanocomposite for efficient electrocatalysis of oxygen reduction, ACS Appl. Mater. Inter. 8 (2016) 32307–32316.
[50] Q. Li, W. Chen, H. Xiao, Y. Gong, Z. Li, L. Zheng, X. Zheng, W. Yan, W. Cheong, R. Shen, N. Fu, Z. Zhuang, C. Chen, D. Wang, Q. Peng, J. Li, Y. Li, Fe isolated single atoms on S, N codoped carbon by copolymer pyrolysis strategy for highly efficient oxygen reduction reaction, Adv. Mater. 30 (2018) 1800588.
[51] G. Ren, X. Lu, Y. Li, Y. Zhu, L. Dai, L. Jiang, Porous core-shell Fe_3C embedded N-doped carbon nanofibers as an effective electrocatalysts for oxygen reduction reaction, ACS Appl. Mater. Inter. 8 (2016) 4118–4125.
[52] B. Chen, Z. Zhang, S. Kim, M. Baek, D. Kim, K. Yong, A biomimetic nanoleaf electrocatalyst for robust oxygen evolution reaction, Appl. Catal. B: Environ. (2019) 118017.
[53] Y. Zhou, Y. Wu, P. Zhang, J. Chen, B. Qu, J.T. Li, Co_3O_4@(Fe-doped) $Co(OH)_2$ microfibers: facile synthesis, oriented-assembly, formation mechanism, and high electrocatalytic activity, ACS Appl. Mater. Inter. 9 (2017) 30880–30890.
[54] S.J. Kim, J. Mahmood, C. Kim, G.F. Han, S. Kim, S.M. Jung, G. Zhu, J.J.D. Yoreo, G. Kim, J.B. Baek, Defect-free encapsulation of Fe^0 in 2D fused organic networks as a durable oxygen reduction electrocatalyst, J. Am. Chem. Soc. 140 (2018) 1737–1742.
[55] M. Qian, S. Cui, D. Jiang, L. Zhang, P. Du, Highly efficient and stable water-oxidation electrocatalysis with a very low overpotential using FeNiP substitutional-solid-solution nanoplate arrays, Adv. Mater. 29 (2017) 1704075.
[56] H. Sun, X. Xu, Z. Yan, X. Chen, F. Cheng, P.S. Weiss, J. Chen, Porous multishelled Ni_2P hollow microspheres as an active electrocatalyst for hydrogen and oxygen evolution, Chem. Mater. 29 (2017) 8539–8547.
[57] Y. Yang, L. Dang, M. Shearer, H. Sheng, W. Li, J. Chen, P. Xiao, Y. Zhang, R.J. Hamers, S. Jin, Highly active trimetallic NiFeCr layered double hydroxide electrocatalysts for oxygen evolution reaction, Adv. Energy Mater. 8 (2018) 1703189.
[58] H. Tan, J. Tang, J. Henzie, Y. Li, X. Xu, T. Chen, Z. Wang, J. Wang, Y. Ide, Y. Bando, Y. Yamauchi, Assembly of hollow carbon nanospheres on graphene nanosheets and creation of iron-nitrogen-doped porous carbon for oxygen reduction, ACS Nano 12 (2018) 5674–5683.
[59] S. Dutta, A. Indra, Y. Feng, H. Han, T. Song, Promoting electrocatalytic overall water splitting with nanohybrid of transition metal nitride-oxynitride, Appl. Catal. B: Environ. 241 (2019) 521–527.
[60] L. Xu, Q. Jiang, Z. Xiao, X. Li, J. Huo, S. Wang, L. Dai, Plasma-engraved Co_3O_4 nanosheets with oxygen vacancies and high surface area for the oxygen evolution reaction, Angew. Chem. Int. Ed. 55 (2016) 5277–5281.
[61] S. Zhao, Y. Wang, J. Dong, C. He, H. Yin, P. An, K. Zhao, X. Zhang, C. Gao, L. Zhang, J. Lv, J. Wang, J. Zhang, A.M. Khattak, N.A. Khan, H. Wei, J. Zhang, S. Liu, H. Zhao, Z. Tang, Ultrathin metal-organic framework nanosheets for electrocatalytic oxygen evolution, Nat. Energy 1 (2016) 16184.
[62] Q. Qin, H. Jang, P. Li, B. Yuan, X. Liu, J. Cho, A tannic acid-derived N-, P-codoped carbon-supported iron-based nanocomposite as an advanced trifunctional electrocatalyst for the overall water splitting cells and zinc-air batteries, Adv. Energy Mater. 9 (2019) 1803312.
[63] Y. Pan, K. Sun, S. Liu, X. Cao, K. Wu, W.C. Cheong, Z. Chen, Y. Wang, Y. Li, Y. Liu, D. Wang, Q. Peng, C. Chen, Y. Li, Core-shell ZIF-8@ ZIF-67-derived CoP nanoparticle embedded N-doped carbon nanotube hollow polyhedron for efficient overall water splitting, J. Am. Chem. Soc. 140 (2018) 2610–2618.
[64] Y. Lin, Z. Tian, L. Zhang, J. Ma, Z. Jiang, B.J. Deibert, R. Ge, L. Chen, Chromium-ruthenium oxide solid solution electrocatalyst for highly efficient oxygen evolution reaction in acidic media, Nat. Comm. 10 (2019) 162.
[65] Y. Wang, B. Kong, D. Zhao, H. Wang, C. Selomulya, Strategies for developing transition metal phosphides as heterogeneous electrocatalysts for water splitting, Nano Today 15 (2017) 26–55.
[66] A. Kramida, Y. Ralchenko, J. Reader, NIST Atomic Spectra Database (ver. 5.6.1), accessed: https://physics.nist.gov/asd [2019, April 2].
[67] G. Nave, S. Johansson, Astrophys. The spectrum of Fe II, Astrophys. J. Suppl. S 204 (2013) 1–8.
[68] J. Sugar, C. Corliss, NIST atomic spectra database (ver. 5.6.1), C. J. Phys. Chem. Ref. (Suppl. 2) (1985) 1–664 Data 14 accessed: https://physics.nist.gov/asd [1985, 14].